Article

Not peer-reviewed version

Likely Pathogenicity of Uncharacterized KCNQ1 and KCNE1 Variants

Svetlana I Tarnovskaya and Boris S Zhorov *

Posted Date: 3 June 2025

doi: 10.20944/preprints202506.0195.v1

Keywords: sequence analysis; variant annotation; protein structure; disease informatics; paralogue; missense variants

 doi:10.20944/preprints202506.0195.v1

Article

Likely Pathogenicity of Uncharacterized KCNQ1 and KCNE1 Variants

Svetlana I. Tarnovskaya [1] and Boris S. Zhorov [1,2,*]

[1] Sechenov Institute of Evolutionary Physiology & Biochemistry, Russian Academy of Sciences, St. Petersburg 194223

[2] Department of Biochemistry and Biomedical Sciences, McMaster University, Hamilton, L8S 4K1, Canada

* Correspondence: zhorov@mcmaster.ca

Abtract: Background: Voltage-gated potassium channels Kv7.1 encoded by gene KCNQ1 play critical roles in various physiological processes. In cardiomyocytes, complex Kv7.1-KCNE1 mediates the slow component of delayed rectifier potassium current that is essential for the action potential repolarization. Over 1,000 KCNQ1 missense variants, many of which are associated with long QT syndrome, are reported in ClinVar and other databases. However, over 600 variants are of uncertain clinical significance (VUS), have conflicting interpretations of pathogenicity or lack germline information. Computational prediction of damaging potential of such variants is important for diagnostics and treatment of cardiac disease. **Methods and Results:** We collected 1,750 benign and pathogenic missense variants of Kv channels from databases ClinVar, Humsavar and Ensembl Variation and tested 26 bioinformatics tools in their ability to identify known damaging variants. The best-performing tool, AlphaMissense, correctly predicted pathogenicity of 195 VUSs in Kv7.1. Among these, 79 variants of 66 wildtype residues (WTRs) are also reported as pathogenic or likely pathogenic (P/LP) in sequentially matching positions of at least one paralogue of hKv7.1. In available cryoEM structures of Kv7.1 with activated and deactivated voltage sensing domains, 52 WTRs form intersegment contacts with WTRs of ClinVar-listed variants, including 21 WTRs with P/LP variants. Analysis of state-dependent contacts suggests atomic mechanisms of dysfunction for some variants. ClinPred and paralogues annotation methods consensually predicted that 21 WTRs of KCNE1 have 34 VUSs with damaging potential. Among these, eight WTRs are contacting 23 Kv7.1 WTRs with 13 ClinVar-listed variants in AplhaFold3 model. **Conclusions:** Bioinformatics tools, including the paralogue annotation method, predicted likely pathogenicity of 79 VUSs in Kv7.1 and 34 VUSs in KCNE1. Analysis of intersegment contacts in CryoEM and AplhaFold3 structures suggests atomic mechanism of dysfunction for some VUSs.

Keywords: sequence analysis; variant annotation; protein structure; disease informatics; paralogue; missense variants

1. Introduction

Voltage-gated potassium channels Kv7.1 encoded by gene KCNQ1 play important roles in physiology and pathophysiology of the heart (Wu and Larsson, 2020; Kekenes-Huskey et al., 2022). Homotetrameric Kv7.1 associated with different beta subunits, which are encoded by KCNE genes, is expressed in various organs including colon, kidney, stomach, inner ear and testis, for reviews see (Jespersen et al., 2005; Abbott, 2014). In the heart, hKv7.1 permeates slow-delayed rectifier potassium current I_{Ks}, which is essential the normal cardiac rhythm (Sanguinetti and Seebohm, 2021). Mutations in the KCNQ1 gene are associated with several heart diseases (Abbott, 2014), including long QT syndrome (Sun and MacKinnon, 2017; Bains et al., 2024), short QT syndrome (Bellocq et al., 2004; Rothenberg et al., 2016), atrial fibrillation (Chen et al., 2003; Hateley et al., 2021) and sudden cardiac death (Albert et al., 2010; Campuzano et al., 2015). Recently, Kv7.1 was found to mediate sex-dependent cold sensation (Kiper et al., 2024).

 doi:10.20944/preprints202506.0195.v1

Each Kv7.1 subunit has six transmembrane (TM) segments. Segments S1 to S4 form the voltage-sensing domain (VSD). Segments S5 and S6 with membrane-reentrant P-loop between them contribute a quarter to the pore domain. The C-terminal domain, which is critical for the channel tetramerization, binds calmodulin that regulates gating (Sachyani et al., 2014). KCNE1 is the primary accessory subunit for the cardiac channel Kv7.1 (Wrobel et al., 2012).

As of March 6, 2025, the ClinVar database lists about 1,000 disease-associated missense variants of KCNQ1. Among these, 519 variants are of unknown clinical significance (VUSs), 131 variants are reported with conflicting interpretations of pathogenicity (CIP), and germline classification is not provided (NP) for 70 variants. The most common diseases associated with Kv7.1 variants are Long QT syndrome (Huang et al., 2018) and short QT interval syndrome (Bellocq et al., 2004). The KCNE1 β subunit has only 103 residues, but as many as 624 missense variants are reported in ClinVar. Among these, 100 variants are VUSs, 21 variants are CIPs, and 24 are NP variants. Artificial neuronal networks have been used to predict some biophysical characteristics of KCNE1 variants (Phul et al., 2022). Functional studies, including high throughput electrophysiology were employed to reclassify many Kv7.1 VUSs as P/LP variants (Vanoye et al., 2018) and reveal molecular mechanisms underlying pathogenicity (Brewer et al., 2025). Nevertheless, large number of still uncharacterized VUSs motivates application of computational methods to predict their pathogenicity.

The American College of Medical Genetics and Genomics and the Association for Molecular Pathology recommend using *in silico* predictive algorithms for interpretation of variants. Various bioinformatics tools based on different principles have been developed to predict pathogenicity and tolerance of genetic variants, with success rates ranging between 60 and 80%. The performance of *in silico* tools may depend on the disease phenotype. For instance, MetaLR, MetaSVM, and MCap have shown top performance in predicting pathogenicity for variants associated with cardiovascular abnormalities. However, some methods yielded many false-positive and false-negative predictions of pathogenicity in individual protein families. Thus, MetaSVM predicted a pathogenic effect for 75% of benign variants of the cardiac sodium channel Nav1.5. Selecting a tool with a high success rate of correct predictions for specific protein families and adjusting the pathogenicity threshold can improve predictions.

Previously, we used various bioinformatics tools combined with the paralogue annotation method (Walsh et al., 2014) to reclassify as P/LP variants numerous VUSs of cardiac sodium channel Nav1.5 (Tarnovskaya et al., 2020), calcium channel Cav1.2 (Tarnovskaya et al., 2021) and TRPM4 channel (Tarnovskaya et al., 2023). The paralogue annotation method employs a multiple sequence alignment of functionally and structurally related proteins, focusing on residues in sequentially matching positions where a disease mutation is known for at least one family member. A VUS in the matching position of the channel under investigation is then predicted as P/LP variant.

In this study, we collected 1,750 benign and pathogenic missense variants of Kv channels from several databases and tested 26 bioinformatics tools in identifying damaging variants. The best-performing tool, AlphaMissense, in combination with the paralogues annotation method predicted pathogenicity of 79 variants. We further used another tool, ClinPred in combination with paralog annotations to predict 34 VUSs of 21 WTRs in KCNE1. In available cryoEM structures of Kv7.1 with activated and deactivated voltage sensing domains and in the AlphaFold model of KCNE1-bound Kv7.1, 52 WTRs of LP-reclassified variants form intersegment contacts with ClinVar-listed WTRs, including 21 WTRs with P/LP variants. Analysis of state-dependent contacts in the cryoEM structures and AlphaFold model suggests atomic mechanism of dysfunction for some variants.

2. Results and Discussions

2.1. Universal Residue Labels of Kv7.1 and Its Paralogs

In this study we show UniProt residue numbers of Kv7.1 and its paralogues as well as PLIC labels, which are universal for P-Loop Ion Channels (Tikhonov et al., 2025). A PLIC label refers to the segment, the channel subunit (when necessary), and residue position relative to the reference residue

 doi:10.20944/preprints202506.0195.v1

in the segment, which is most conserved in the multiple sequence alignment of P-loop channels. The reference residues have numbers 550 in TM helices or 850 in P-loops. Subunits are designated "A", "B", "C" and "D". When viewed from the extracellular side, subunits A to D are arranged clockwise (Gigolaev et al., 2025). PLIC labels facilitate recognition of residue locations in different P-loop channels. Several 3D-aligned structures of Kv7.1 and Kv7.2 channels with PLIC labels are available in database https://plic3da.com. Supplemental file PLIC_Uniprot_Kv.xlsx provides relations between PLIC labels and UniProt numbers for potassium channels mentioned in this study.

2.2. Composing a Broad Dataset of Missense Variants for Channel hKv7.1 and Its Paralogues

According to the Ensemble database, there are 31 paralogues of KCNQ1 (ENSG00000053918), but only 14 of them contain P/LP variants that are used in the paralog annotation method. For KCNQ1 and its 14 paralogues (Table 1), we collected a total of 5,632 missense variants from the gnomAD, ClinVar, Ensembl, and Humsavar databases (Table S1). These include 1,059 P/LP variants, 691 common neutral variants (with AF > 0.00001), and 3,882 uncharacterized variants or VUSs. We refer to this dataset as the "broad dataset." The largest numbers of P/LP variants (394) were identified in KCNQ2. For the hKv7.1 channel, we found 299 P/LP variants, 43 benign variants (with AF > 0.00001), and 519 VUSs (Tables 1 and S1).

Table 1. Known missense variants of hKv7.1 and its paralogues.

Gene [a]	UniProt ID[b]	P/LP [c]	VUS [d]	Common neutral [e]
KCNA1	Q09470	38	245	14
KCNA2	P16389	44	207	10
KCNA5	P22460	4	276	56
KCNB1	Q14721	87	212	62
KCNC1	P48547	11	149	11
KCNC2	Q96PR1	12	44	37
KCNC3	Q14003	10	173	82
KCND2	Q9NZV8	7	176	22
KCND3	Q9UK17	21	207	17
KCNQ1	P51787	299	519	43
KCNQ2	O43526	394	474	57
KCNQ3	O43525	39	458	49
KCNQ4	P56696	28	153	63
KCNQ5	Q9NR82	20	228	65
KCNV2	Q8TDN2	45	361	103

[a] Genes of voltage-gated potassium ion channels, which have P/LP variant(s) in public databases; [b] Accession number of a protein in the UniprotKB database; [c] Number of P/LP variants; [d] Number of variants of unknown clinical significance; [e] Number of variants from the gnomAD database, which occur in a population with allele frequency > 0.00001 and are absent in the ClinVar database.

2.3. Distribution of Missense Variants in Topological Regions of hKv7.1

Many pathogenic variants are localized in the C-terminal region and P-loop of the channel. Most of P/LP variants are associated with the long QT syndrome 1 (LQT1).

 doi:10.20944/preprints202506.0195.v1

2.4. Comparing Performance of Bioinformatics Tools

We have chosen only those tools, which predicted pathogenicity for > 70% variants in our dataset. Thus, we excluded from our analysis algorithms EVE, MutPred, and MutationTaster. To compare performance of 26 deleteriousness prediction scores (Table 2), we compiled a test set with 691 true positive (TP) and 1,059 true negative (TN) observations obtained from our broad dataset (Table S1). Pre-computed algorithm scores were retrieved from database dbNSFP v4.5. For each tool, we determined the optimal pathogenicity threshold and calculated sensitivity, specificity, and accuracy (Table 2). We used the area under the Receiver Operating Characteristic (ROC) curve as the performance measure (Figure 1A).

A

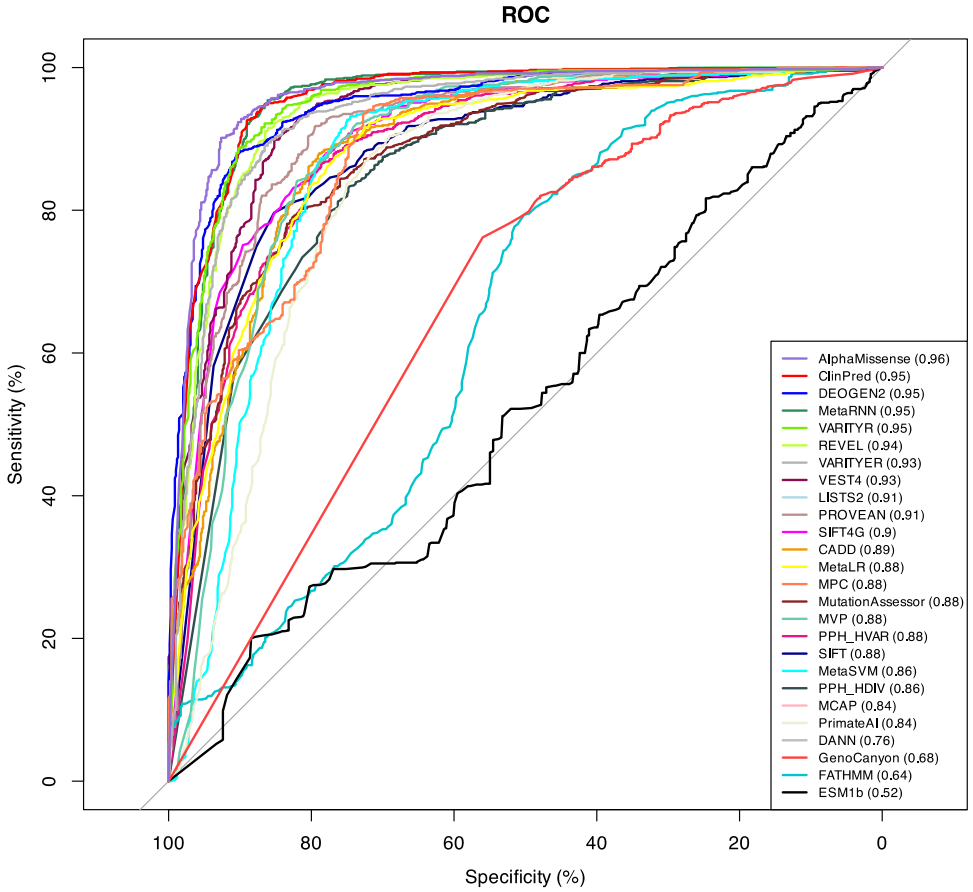

 doi:10.20944/preprints202506.0195.v1

B

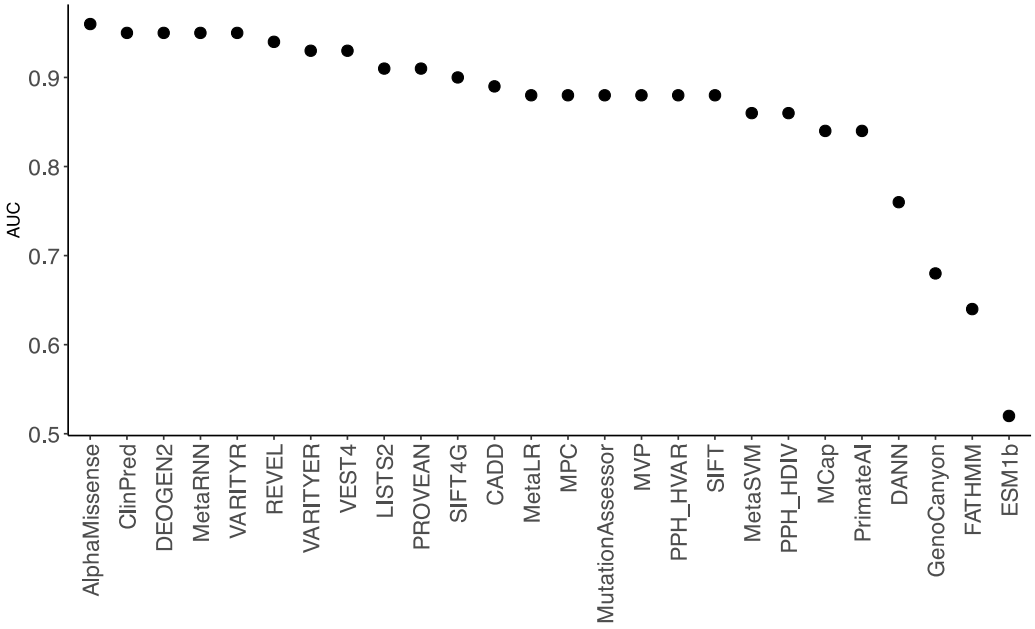

Figure 1. A. ROC curves for prediction algorithms on the broad dataset illustrate performance of quantitative predictions. The larger is the area under the ROC curve (AUC) the better is the algorithm performance. **B.** AUC values arranged to decrease from the best-performing algorithm (AlphaMissense) to the worst-performing algorithm (ESMB1b).

Table 2. Performance of variant interpretation tools.

Tool	Deleterious Threshold [a]	Sensitivity [b]	Specificity [c]	MCC [d]	ACC [e]	AUC [f]
AlphaMissense	>0.5	0.95	0.86	0.81	0.9	0.96
ClinPred	>0.8	0.97	0.79	0.77	0.87	0.95
DEOGEN2	>0.5	0.96	0.67	0.65	0.81	0.95
MetaRNN	>0.6	0.97	0.82	0.79	0.89	0.95
VARITYR	>0.5	0.93	0.86	0.78	0.89	0.95
REVEL	>0.45	0.99	0.56	0.59	0.76	0.94
VARITYER	>0.5	0.9	0.85	0.75	0.87	0.93
VEST4	>0.5	0.97	0.73	0.72	0.85	0.93
LISTS2	>0.85	0.97	0.54	0.55	0.73	0.91
PROVEAN	<-1.5	0.96	0.62	0.61	0.78	0.91
SIFT4G	<0.05	0.9	0.75	0.65	0.82	0.9
CADD	>3	0.93	0.68	0.63	0.8	0.89
MetaLR	>0.4	0.99	0.15	0.25	0.54	0.88
MPC	>2	0.57	0.92	0.51	0.74	0.88
MutationAssessor	>1.7	0.89	0.68	0.58	0.78	0.88
MVP	>0.75	0.99	0.43	0.49	0.68	0.88
PPH_HVAR	>0.45	0.91	0.69	0.61	0.79	0.88
SIFT	<0.0045	0.82	0.8	0.62	0.81	0.88

 doi:10.20944/preprints202506.0195.v1

MetaSVM	>0	0.99	0.28	0.37	0.61	0.86
PPH_HDIV	>0.45	0.93	0.56	0.52	0.73	0.86
MCap	>0.05	1	0.19	0.31	0.57	0.84
PrimateAI	>0.6	0.98	0.46	0.5	0.7	0.84
DANN	>0.5	1	0.04	0.14	0.52	0.76
GenoCanyon	>0.7	0.89	0.35	0.29	0.62	0.68
FATHMM	<-1	0.99	0.08	0.18	0.5	0.64
ESM1b	<-3	0.69	0.35	0.05	0.51	0.52

[a] Deleterious threshold is the custom pathogenicity threshold that divides variants in two categories: pathogenic or benign. The larger or smaller the score than the threshold, the more likely the variant is damaging. [b] Sensitivity characterizes the number of P/LP variants, which were predicted as P/LP by the tool. [c] Specificity characterizes number of benign variants, which were predicted as benign by the tool. [d] MCC, Matthews Correlation Coefficient. [e] ACC, Accuracy indicates the predictive accuracy of the tool. [f] AUC, Area under the ROC curve.

AlphaMissense and ClinPred demonstrated the best performance (AUC = 0.96) in the broad dataset (Figure 1), followed by VARITYR (AUC = 0.95), MetaRNN (AUC = 0.95), and DEOGEN2 (AUC = 0.95). AlphaMissense correctly classified 96% of the P/LP variants as pathogenic variants and 85% of the common neutral variants as tolerated variants (Table 2).

DEOGEN2, MetaRNN, and VARITYR also have high predictive parameters with AUC = 0.95. The lowest accuracy across all methods was found for ESM1b (AUC = 0.52), FATHMM (0.64), and GenoCanyon (0.68). The results indicate that AlphaMissense and ClinPred are the best-performing pathogenicity predictors for variants in the Kv family.

2.5. Paralogue Annotation of Kv7.1 Variants

Using multiple sequence alignments of hKv7.1 and its paralogues, we mapped each residue with a known P/LP variant from a paralogue protein onto the corresponding amino acid position of hKv7.1. A total of 555 known P/LP variants in paralogues were mapped to 195 amino acid positions in the hKv7.1 channel (Table S2). In these positions, we found 410 variants of hKv7.1, including 174 VUSs, 226 P/LP variants, and 10 common neutral variants. In some cases, multiple variants were mapped to the same sequence position. Forty-three P/LP variants of paralogues were mapped to the P-loop region of hKv7.1, forty-seven P/LP paralogue variants to the C-terminal region, and twenty-four P/LP variants to the S4 segment (Table S2).

2.6. AlphaMissense and Paralogues Annotations Consensually Predicted Pathogenicity of 79 VUS

As many as 519 variants of Kv7.1 in our dataset are currently classified as VUSs (Table 1). We used the best-performing tool, AlphaMissense, to predict pathogenicity of these VUSs. AlphaMissense identified 195 VUSs with a pathogenicity threshold > 0.5 as P/LP variants. Among these, we further selected those variants that are annotated as P/LP in at least one of the fourteen paralogs of hKv7.1 (Table 1) with a conservation score across paralogs Cs > 0.3. Both methods consensually predicted 79 P/LP variants (Table 3). Among these only 6 variants are functionally characterized by high-throughput functional analysis (Vanoye et al., 2018). Five of these have a very strong decrease of the current density and one shows a moderate decrease (Table 3). These experimental data confirm the predictive power of our approach. Below we describe intersegment contacts of WTRs for some LP-reclassified VUSs that may guide their selection for functional studies.

 doi:10.20944/preprints202506.0195.v1

Table 3. hKv7.1 VUSs reclassified as LP variants [a].

PLIC Label	hKv7.1 variant	Paralog	ClinPred	α missense	Current Change [b]
1.532	$E^{115}D$	KCNQ2-$E^{86}K$	0.878	0.997	
1.545	$A^{128}P$	KCNQ2-$Y^{98}X$	0.185	0.861	
1.548	$L^{131}P$	KCNQ2-$L^{101}H$	0.995	0.958	↓↓
1.550	$V^{133}A$	KC NA1-$I^{177}N$,KCNB1-$I^{199}F$, KCNQ2-$V^{103}D$	0.984	0.964	↓
1.553	$C^{136}F$	KCNQ2-$C^{106}G$	1	0.954	↓↓
1.554	L^{137} P	KCNQ2-$L^{107}F$	0.986	0.999	
1.557	$S^{140}R$	KCNA1-$F^{184}C$	0.996	0.999	↓↓
1.560	$S^{143}F$	KCNB1-$N^{209}K$	0.997	0.953	
2.544	$V^{164}A$	KCNQ2-$I^{134}N$	0.998	0.797	
2.550	$E^{170}G$	KCNQ2-$E^{140}A$	1	0.987	
2.551	$Y^{171}H$	KCNV2-$Y^{317}X$	0.998	0.998	
2.556	$W^{176}S$	KCNQ2-$W^{146}X$	1	0.926	
2.609	$G^{189}A$	KCNQ2-$G^{159}E/R/V$	0.998	0.978	↓↓
3.549	$I^{201}V$	KCNA2-$I^{258}N$	0.944	0.507	
3.550	$D^{202}V$	KCNQ2-$D^{172}G$	1	0.998	
3.560	$V^{212}A$	KCNQ2-$V^{182}M$	0.994	0.958	
3.560	$V^{212}F$	KCNQ2-$V^{182}M$	0.997	0.917	
3.600	$G^{219}E$	KCNA1-$E^{283}K$,KCNQ2-$G^{189}D$	0.989	0.817	
4.542	$A^{223}T$	KCNQ2-$A^{193}D/V$	0.994	0.772	
4.547	$R^{228}W$	KCNA2-$R^{294}H$,KCNQ2-$R^{198}W$	1	0.966	
4.553	$Q^{234}L$	KCNA2-$R^{300}S$, KCNB1-$R^{303}Q$, KCNC3-$R^{420}H$, KCNQ2-$Q^{204}H$	0.998	0.965	
4.553	$Q^{234}R$	KCNA2-$R^{300}S$, KCNB1-$R^{303}Q$, KCNC3-$R^{420}H$, KCNQ2-$Q^{204}H$	0.97	0.992	
4.558	$L^{239}V$	KCNQ2-$I^{209}S/T$	0.829	0.86	
4.559	$H^{240}R$	KCNQ2-$R^{210}C/H/P$	0.331	0.949	
4.559	$H^{240}Q$	KCNQ2-$R^{210}C/H/P$	0.993	0.991	
5.518	$G^{245}R$	KCND3-$S^{304}F$	0.998	0.998	↓↓
5.523	$L^{250}P$	KCNA1-$I^{314}T$,KCNB1-$S^{319}F/Y$	0.995	1	
5.525	$G^{252}R$	KCNB1-$G^{321}S$	1	0.996	
5.525	$G^{252}S$	KCNB1-$G^{321}S$	0.998	0.885	
5.526	$S^{253}A$	KCNQ2-$S^{223}F/P$	0.972	0.792	
5.530	$I^{257}S$	KCNQ2-$A^{227}V$	0.993	0.947	
5.533	$Q^{260}H$	KCNQ2-$K^{230}M$	0.991	0.99	
5.535	$L^{262}V$	KCNC3-$F^{448}L$	0.996	0.952	
5.536	$I^{263}K$	KCNB1-$G^{332}V$	0.997	0.997	
5.537	$T^{264}S$	KCNQ2-$T^{234}A/P$	0.992	0.895	
5.540	$Y^{267}F$	KCNQ2-Y237C	0.996	0.644	
5.541	$I^{268}V$	KCNC2-$F^{388}S$	0.878	0.674	
5.548	$F^{275}L$	KCNQ2-L245P	0.996	0.986	
5.552	$F^{279}C$	KCND3-$V^{338}E$,KCNQ2-$L^{249}P$	0.999	0.788	
5.556	$A^{283}T$	KCNQ2-$A^{253}S/T$	0.996	0.504	
5.557	$E^{284}G$	KCNQ2-$E^{254}D$	1	0.972	
5.613	$S^{298}R$	KCNQ2-$T^{263}A/I$	0.997	0.977	
5.837	$A^{300}G$	KCNQ2-$A^{265}P/T/V$	0.986	0.747	
5.843	$G^{306}E$	KCNQ2-$G^{271}D/R/S/V$, KCNQ3-$G^{310}D/V$	0.999	0.999	
5.844	$V^{307}M$	KCNB1-$T^{372}N/I$	0.991	0.79	
5.844	$V^{307}L$	KCNB1-$T^{372}N/I$	0.99	0.895	
5.844	$V^{307}E$	KCNB1-$T^{372}M/I$	0.993	0.989	
5.849	$T^{312}S$	KCNA2-$T^{374}A$, KCNC2-$T^{437}A$, KCNQ2-$T^{277}N/P/S$	0.995	0.966	
5.850	$I^{313}F$	KCNQ2-$I^{278}F/M/T$, KCNQ3-$I^{317}M/T$	0.993	0.991	
5.855	$K^{318}N$	KCNQ2-$K^{283}E$	0.958	0.93	
5.856	$V^{319}M$	KCNQ2-Y284C/D	0.995	0.616	
6.543	$A^{329}V$	KCND3-G384S, KCNQ2-A294G/S	0.999	0.979	
6.543	$A^{329}T$	KCND3-G384S,KCNQ2-A294G/S	0.987	0.935	
6.544	$S^{330}Y$	KCND3-S385P	0.998	0.993	
6.545	$C^{331}Y$	KCNQ2-T296P	0.998	0.976	
6.549	$F^{335}C$	KCNA1-A395S	0.997	0.856	
6.551	$I^{337}M$	KCNA2-V399M	0.962	0.775	

 doi:10.20944/preprints202506.0195.v1

6.553	F^{339}V	KCNQ2-F^{304}C,KCNQ2-F^{304}S	0.999	0.972
6.555	A^{341}T	KCNA1-A^{401}V, KCNB1-A^{406}V, KCNQ2-A^{306}P/T/V/E	0.996	0.976
6.563	S^{349}A	KCNB1-N^{414}D	0.995	0.92
6.563	S^{349}L	KCNB1-N^{414}D	0.999	0.995
6.566	A^{352}P	KCNB1-S^{417}P,KCNQ2-A^{317}T, KCNQ3-A^{356}T	0.999	0.997
6.566	A^{352}D	KCNB1-S^{417}P,KCNQ2-A^{317}T, KCNQ3-A^{356}T	0.998	1
6.569	K^{354}R	KCNQ2-K^{319}E	0.992	0.768
6.571	Q^{357}R	KCNA1-R^{417}X,KCNB1-E^{422}A	0.996	0.984
6.571	Q^{357}E	KCNA1-R^{417}X,KCNB1-E^{422}A	0.939	0.566
6.574	R^{360}T	KCNQ2-R^{325}G,KCNQ3-R^{364}C/H	0.999	0.999
6.574	R^{360}K	KCNQ2-R^{325}G,KCNQ3-R^{364}C/H	0.992	0.976
7.013	L^{374}V	KCNQ2-L^{339}Q,KCNQ2-L^{339}R	0.995	0.85
7.030	T^{391}P	KCNQ2-T^{359}K	0.998	0.898
7.165	K^{526}E	KCNQ2-K^{552}N	0.932	0.967
7.165	K^{526}Q	KCNQ2-K^{552}N	0.838	0.717
7.165	K^{526}N	KCNQ2-K^{552}N	0.984	0.995
7.180	V^{541}I	KCNQ2-V^{567}D	0.903	0.814
7.187	G^{548}D	KCNQ2-G^{574}D/S	0.999	0.999
7.194	R^{555}L	KCNQ2-R^{581}G	0.998	0.994
7.196	K^{557}R	KCNQ2-K^{583}N	0.982	0.63
7.222	R^{583}S	KCNQ2-K^{606}X	0.885	0.902
7.222	R^{583}G	KCNQ2-K^{606}X	0.79	0.606
7.230	R^{591}P	KCNQ2-R^{622}P	0.997	0.997

[a] Shown are PLIC labels that are universal for P-loop channels (Tikhonov et al., 2025) and UniProt residue numbers of specific channels. [b] Current density decreases strongly (↓↓) or moderately (↓) according to (Vanoye et al., 2018).

2.7. Intersegment Contacts Involving WTRs with LP-Reclassified VUSs

Above bioinformatics approaches strongly suggest likely pathogenicity of 79 VUSs in Kv7.1, but molecular mechanisms of the variants' dysfunction are unclear. Analysis of intersegments contacts and their state dependency may suggest mechanisms of stabilization or destabilization of specific channel states that underlie the molecular mechanisms. We this goal in mind, we 3D-aligned cryoEM structures of Kv7.1 with VSDs in the activated (8sik) and deactivated (8sin) states (Mandala and MacKinnon, 2023) as described in Methods. Upon a VSD deactivation, helix S4 undergoes substantial downshift (Figure 2A) and rotation (Figure 2B), while rearrangements of helices S5 and S6 are rather small. In both 8sik and 8sin structures, the pore at the level of serines S$^{6.563}$ is narrow (Figure 3A) implying a closed channel (Mandala and MacKinnon, 2023). Surprisingly, leucines L$^{6.567}$ in the 8sik structure form a much tighter constriction than in 8sin (Figure 3A). However, CA atoms of leucines L$^{6.567}$ in both structures are close to each other and respective CA-CB bonds are collinear (Figure 3A) indicating that the tighter constriction in 8sik is due to the sidechain rotations rather than rearrangement of the S6 bundle.

Co-expression of Kv7.1 with KCNE3 yields constitutively open channels by promoting VSD activation (Barro-Soria et al., 2015; Kasuya and Nakajo, 2022). While VSDs in cryoEM structure (6v01) of KCNE3 bound Kv7.1 are deactivated (Sun and MacKinnon, 2017), the S6 bundle is much wider than that in 8sin (Figure 3b) indicating that KCNE3 binding is sufficient to widen the pore even when VSDs are deactivated. Thus, although cryoEM structures of Kv7.1 with activated VSDs and open pore domain are lacking, available cryoEM structures of Kv7.1 allow analyzing intersegment contacts of WTRs with LP-reclassified VUSs and, to some extent, their state-dependency.

We visualized intersegment contacts in VSDs involving WTRs of LP-reclassified VUSs and WTRs of other ClinVar reported variants in structures with deactivated (Figure 2C) and activated (Figure 2D) VSDs. Since the pore domain and especially its extracellular half is more 3D conserved than VSDs, we analyzed intersegment contacts in the pore domain in structure with deactivated VSDs (Figures 4–6), and then in structure with KCNE1 bound channel. These contacts are listed in Tables 4–7.

 doi:10.20944/preprints202506.0195.v1

The vast majority of Kv7.1 P/LP variants, which are reported in ClinVar, as well as LP-reclassified VUSs (Table 3) are associated with long QT syndrome, indicating that respective mutations destabilize the open channel, decrease the I_{Ks} current, and thus prolong the action potential. In case of cardiac channel Nav1.5, for many intersegment state-dependent contacts involving WTRs with ClinVar reported variants, substitution of either contact partner causes the channel dysfunction associated with the same syndrome (Korkosh et al., 2021). By analogy, we propose that if two WTRs of Kv7.1 form an intersegment contact with one partner reported in ClinVar with P/LP variant and another partner has a LP-reclassified VUS, it strongly increases the reliability of our VUSs reclassification as LP variants.

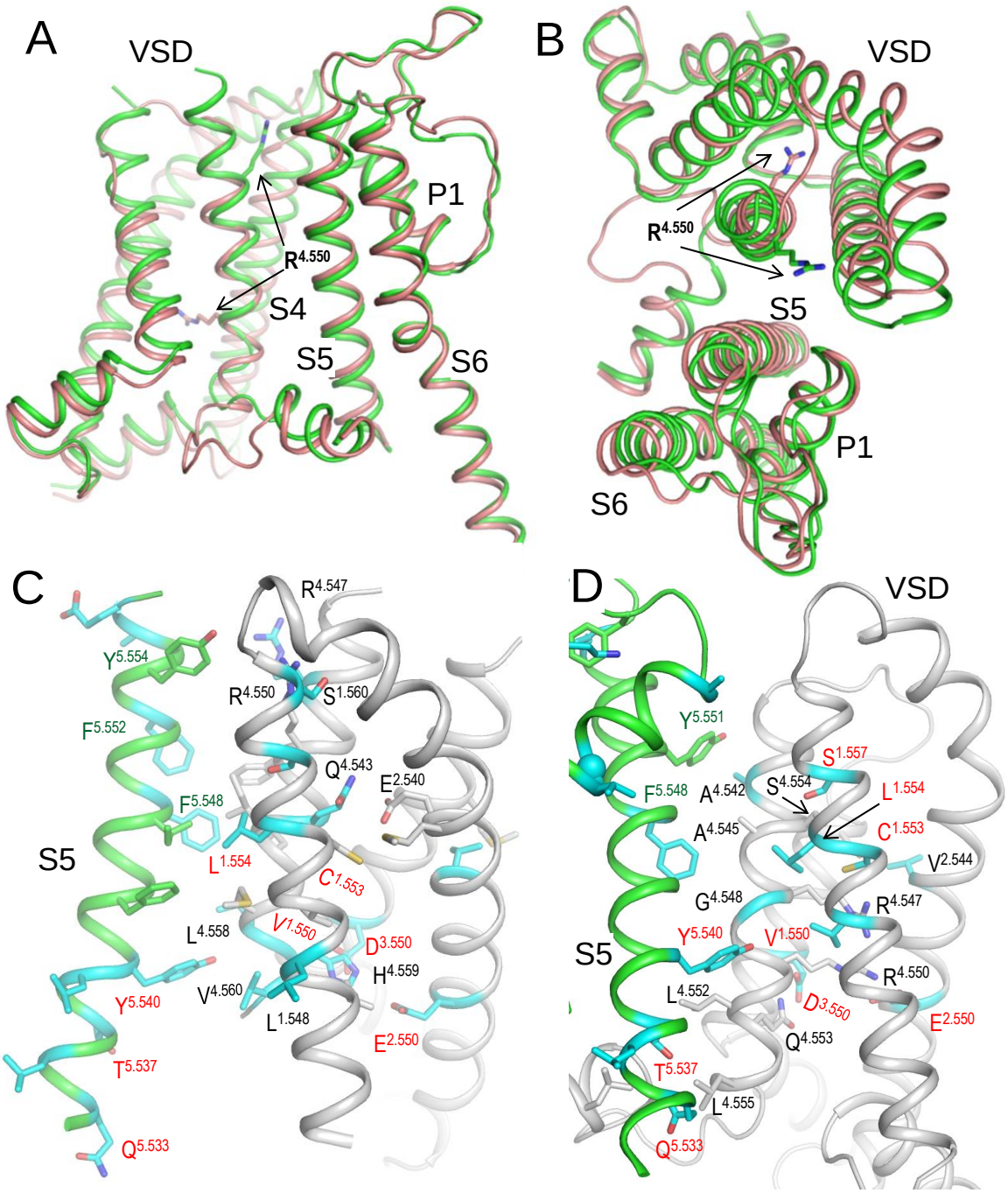

Figure 2. CryoEM structures of hKv7.1. A, B. Side (A) and extracellular (B) views at the interface between a VSD and a quarter of PD in cryoEM structures with activated (green, 8sik) and deactivated (brown, 8sin) VSDs. Note significant downshift of $R^{4.550}$ (A) and its anticlockwise rotation (B) upon VSD deactivation. **C, D.** Intersegment contacts of WTRs with LP-reclassified VUSs (cyan carbons) in the cryoEM structures with activated (C) and

 doi:10.20944/preprints202506.0195.v1

deactivated (D) VSDs. Specific contacts are listed in Tables 4-7. Red labels indicate residues that contact WTRs with known P/LP variants (Table 4).

Table 4. LP-reclassified VUSs whose WTRs contact WTRs of ClinVar-reported P/LP variants [a].

VUS → LP	P/LP	State [b]	VUS → LP	P/LP	State
$V^{133/1.550}A$	$R^{231/4.550}L$	↓	$L^{262/5.535}V$	$P^{343/6.557}A$	↓
	$Q^{234/4.553}P$	↑ o		$P^{343/6.557}A/S$	↑
$C^{136/1.553}F$	$S^{225/4.544}L/W$	↓	$T^{264/5.537}S$	$L^{233/4.552}M$	↓
	$L^{156/2.536}P$	↑ o		$L^{251/5.524}Q/P$	↑
	$Q^{234/4.553}P$	↑		$G^{269/5.542}R/S/V/D$	↑
$L^{137/1.554}P$	$S^{225/4.544}L/W$	↓	$Y^{267/5.540}F$	$G^{229/4.548}D$	↓
	$G^{229/4.548}D$	↓		$L^{233/4.552}M$	↓
	$Q^{234/4.553}P$	↑	$E^{284/5.557}G$	$T^{322/5.859}P/A/R$	↓
	$I^{235/4.554}N$	↑		$P^{320/5.857}S$	↓
	$I^{274/5.547}D$	↑		$G^{325/6.539}W$	
	$R^{231/4.550}S/C/L/H$	o	$G^{306/5.843}E$	$L^{273/5.546}I/V/P/R/F$	↓
	$Q^{234/4.553}P$	o	$V^{307/5.844}M/L/E$	$S^{330/\backslash 6.544}Y$	↓
	$I^{235/4.554}L/N$	o	$T^{312/5.849}S$	$T^{312/5.849}I/S$	↓
$S^{140/1.557}R$	$S^{225/4.544}L/W$	↓	$I^{313/5.850}F$	$G^{314/5.851}R/D/S$	↓
	$L^{156/2.536}P$	↑		$T^{312/5.849}S/I$	↓
	$R^{231/4.550}S/C/L/H$	↑ o		$T^{309/5.846}I$	↓
	$Q^{234/4.553}P$	↑ o	$V^{319/5.856}M$	$Y^{315/5.852}S$	↓
	$L^{156/2.536}P$	o		$W^{304/5.841}R/L/S$	↓
$S^{143/1.560}F$	$R^{231/4.550}S/C/L/H$	o		$W^{304/5.841}$ G	↓
$V^{164/2.544}A$	S $^{209/3.557}$ P	o		$Y^{315/5.852}D$	↓
$E^{170/2.550}G$	$R^{231/4.550}S/H/C/L$	↓	$I^{337/6.551}M$	$F^{340/6.554}L$	↓
$D^{202/3.550}V$	$Q^{234/4.553}P$	↓	$F^{339/6.553}V$	$L^{251/5.524}Q$	↓
	$R^{231/4.550}S/C/L/H$	↓		$L^{251/5.524}P$	↓
	$R^{234/4.562}S/C/L/H/P$	↑	$A^{341/6.555}T$	$A^{344/6.558}E/V$	↓
	$R^{243/4.562}S/C/L/H/P$	o	$S^{349/6.563}A/L$	$G^{345/6.559}R/V/E$	↓
$Q^{260/A5.533}H$	$L^{251/D5.524}Q/P$	↓	$R^{360/6.574}K/T$	$R^{539/7.178}W/Q$	↓
$L^{262/5.535}V$	$P^{343/6.557}A/S$	o	$K^{557/7.196}R$	$R^{555/7.194}S/C$	↓

[a] ClinVar of 04-Mar-2025. [b]↓, contacts in the hKv7.1 cryoEM structure with "down" VSDs (PDB ID: 8sin) (Mandala and MacKinnon, 2023). ↑, contacts in the hKv7.1 cryoEM structure with "up" VSDs (PDB ID: 8sik) (Mandala and MacKinnon, 2023). o, Contacts in hKv7.1-KCNE3-PIP3 cryoEM structure with open PD and "down" VSDs (PD ID: 6v01) (Sun and MacKinnon, 2020).

Such contacts with known P/LP residues involve 31 LP-reclassified VUSs of 21 WTRs, including eight variants in VSD, seven variants in S5, eight variants in P-loop, and eight variants in S6 (Table 4). Contacts within a VSD and between VSD and S5 are clearly state-dependent (cf. Figs. 2C, D). In particular, H-bonds $R^{4.550}$---$S^{1.560}$, $Q^{4.553}$--- $E^{2.540}$, salt bridges $H^{4.559}$: $E^{2.550}$ and $H^{4.559}$: $D^{3.550}$, and hydrophobic interactions $L^{4.558}$: $F^{5.548}$ stabilize the "up" state of S4 and thus activated state of VSD (Figure 2D). Mutations $R^{4.550}L$, $D^{3.550}H$, $Q^{4.553}P$, $E^{2.550}G$ (Table 4), $L^{4.558}V$ and $F^{275/A5.548}S/L$ (Table 7) would weaken or eliminate these contacts and destabilize the activated VSD. This would decrease probability of the channel open state, shorten I_{Ks}, and prolong the action potential in cardiomyocytes, explaining why respective variants are associated with the gain-of-function long QT syndrome. However, some of the above mutations (e.g. $R^{4.550}L$ and $E^{2.550}G$) would also destabilize deactivated VSD (Figure 2D). Therefore, the long QT syndrome associated with these variants indicates that respective mutations destabilize activated state of VSD stronger than its deactivated state.

 doi:10.20944/preprints202506.0195.v1

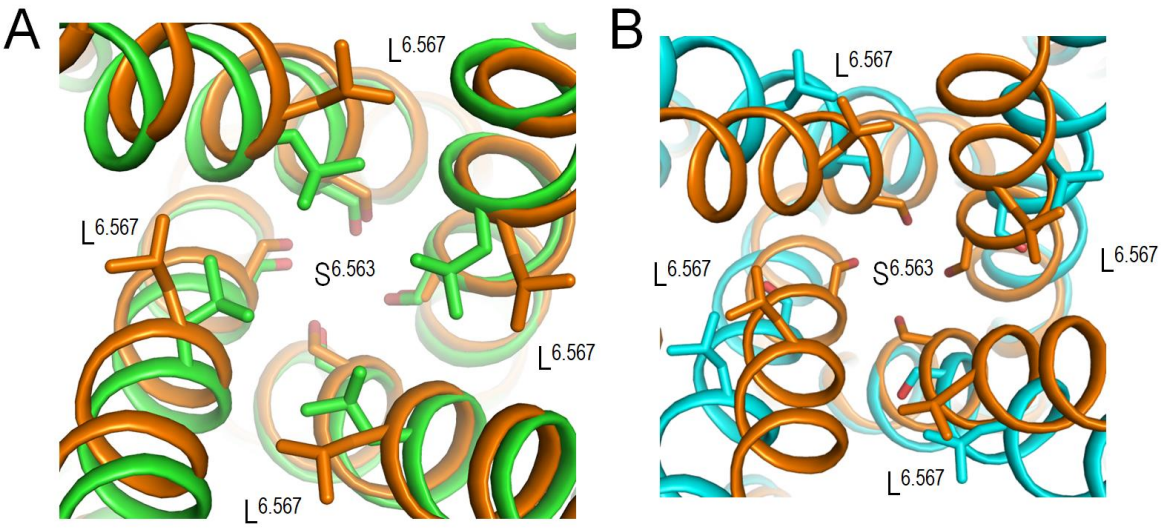

Figure 3. Cytoplasmic views of the Kv7.1 pore lumen in 3D-aligned cryoEM structures. **A**. In structures with activated (8sik, green) and deactivated (8sin, brown) VSDs, the bundle of S6 helices is rather conserved, and the pore-facing serines $S^{6.563}$ apparently block the lumen suggesting the closed channel (Mandala and MacKinnon, 2023). The pore constriction at the level of leucines $L^{6.576}$ in 8sik is narrower than in 8sin, but this difference is mainly due to rotations of the leucine side chains. **B.** In structure with KCNE3 bound Kv7.1 and down VSDs (6v01, cyan) the bundle of S6 helices is much wider than in the Kv7.1 structure with deactivated VSD and without KCNE (8sin, brown). In the former structure, neither $S^{6.563}$ nor $L^{6.567}$ apparently blocks the pore in agreement with the notion that KCNE3 binding creates constitutively open Kv7.1.

Table 5. LP-reclassified VUSs whose WTRs form intersegment contacts with WTRs of other ClinVar-reported VUSs [a].

VUS → LP	Contact		VUS → LP	Contact	
$V^{133/A1.550}I/A$	$R^{228/A4.547}W$	VUS→ LP	$K^{318/A5.855}N$	$D^{301/A5.838}Y$	VUS
	$G^{229/A4.548}S/V$	VUS	$S^{349/A6.563}A/L$	$S^{349/B,D6.563}A/L$	VUS→ LP
	$Y^{267/B5.540}F$	VUS→ LP		$A^{352/B,D6.566}P/D$	VUS→ LP
$C^{136/A1.553}F$	$R^{228/A4.547}W$	VUS→ LP	$A^{352/A6.566}P/D$	$L^{353/B6.567}P$	VUS
$L^{137/A1.554}P$	$G^{229/A4.548}S/V$	VUS		$S^{349/B6.563}A/L$	VUS→ LP
	$R^{228/A4.547}W$	VUS→ LP		$G^{350/B6.564}R$	VUS
$D^{202/A3.550}V$	$Q^{234/A4.553}L/R$	VUS→ LP	$R^{360/A6.574}K/T$	$P^{535/A7.174}T$	VUS
$S^{253/A5.526}A$	$K^{354/A6.568}R$	VUS→ LP	$T^{391/A7.030}P$	$R^{518/A7.157}Q/P$	VUS
$Y^{267/A5.540}F$	$G^{229/D4.548}S/V$	VUS	$V^{541/A7.180}I$	$V^{541/B,D7.180}I$	VUS→ LP
$E^{284/A5.557}G$	$V^{324/6.538}L/I/F$	VUS		$Y^{545/B7.184}F$	VUS
$A^{300/A5.837}S/G$	$K^{326/B6.540}E$	VUS	$G^{548/A7.187}D$	$Y^{545/B7.184}F$	VUS
$T^{312/A5.849}S$	$I^{313/5.850}F$	VUS→ LP			
	$I^{337/A6.551}M$	VUS→ LP			

[a] ClinVar Data on 04-Mar-2025; [b] In the cryoEM structure of hKv7.1 (PDB ID: 8sin) with voltage sensor in the down state (Mandala and MacKinnon, 2023); [c] CIP, Conflicting interpretations of pathogenicity; NP, data not provided.

 doi:10.20944/preprints202506.0195.v1

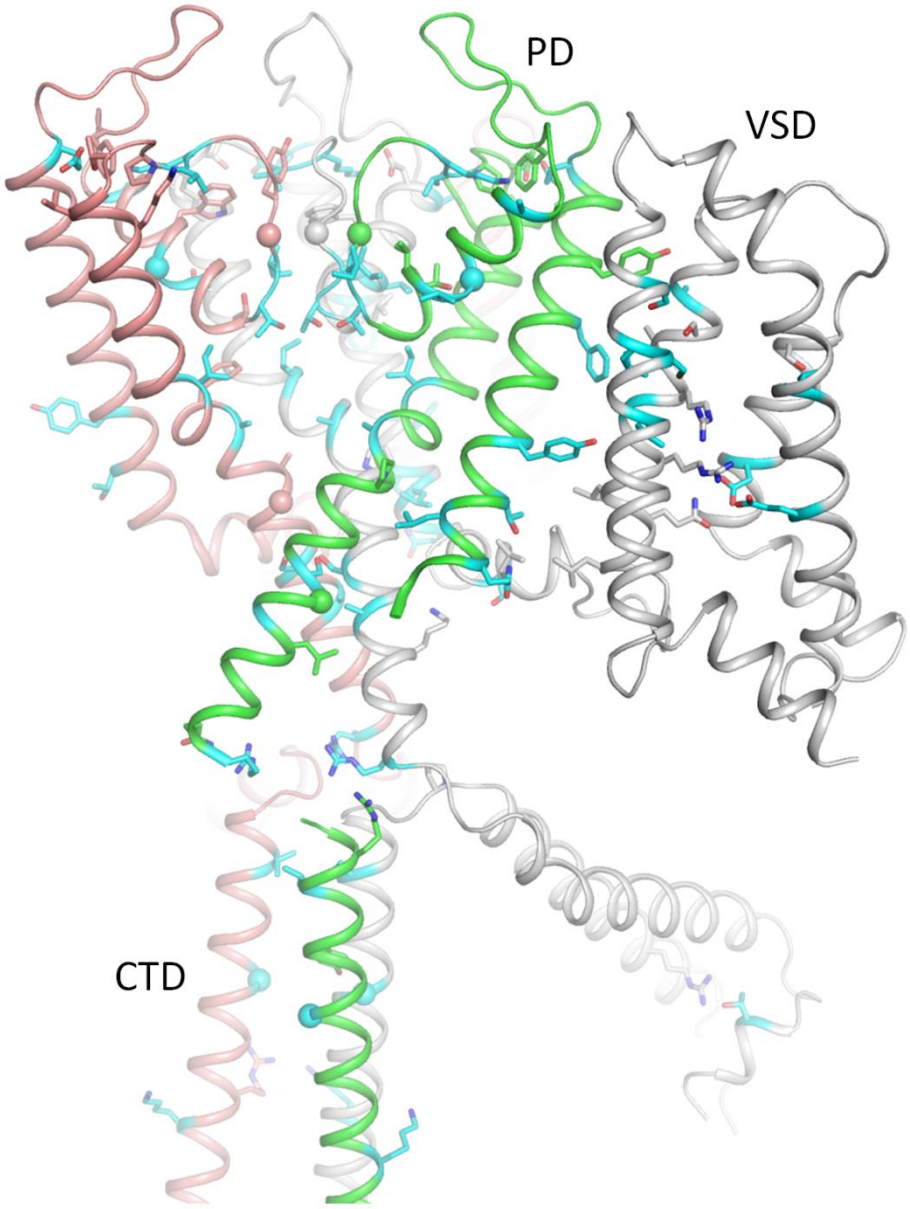

Figure 4. CryoEM structure of hKv7.1 with VSDs in the down state (PDB ID: 8sin). Subunit C and some other parts of the channel are removed for clarity. Subunits A, B and D are gray, green and brown, respectively. WTRs involved in intersegment contacts (Tables 4-7) are shown as sticks (CA atoms of glycines are spheres). WTRs of VUSs reclassified LP variants (Table 3) are shown with cyan carbons, and their contact WTRs with ClinVar-listed variants are shown with carbons colored as respective ribbons. Close-up views of specific contacts are given in Figures 5 and 6.

Table 4 also shows seven LP-reclassified VUSs in the cytoplasmic part of S6 (positions 6.553 - 6.574) and six LP-reclassified VUSs in the cytoplasmic part of S5 (positions 5.533 -5.540). These residues undergo substantial movements upon the activation gating implying that respective disease mutations destabilize the channel open state. Importantly, WTRs of respective variants contact WTRs with ClinVar reported P/LP variants (Table 4). These residues are marked with red labels in Figure 4.

 doi:10.20944/preprints202506.0195.v1

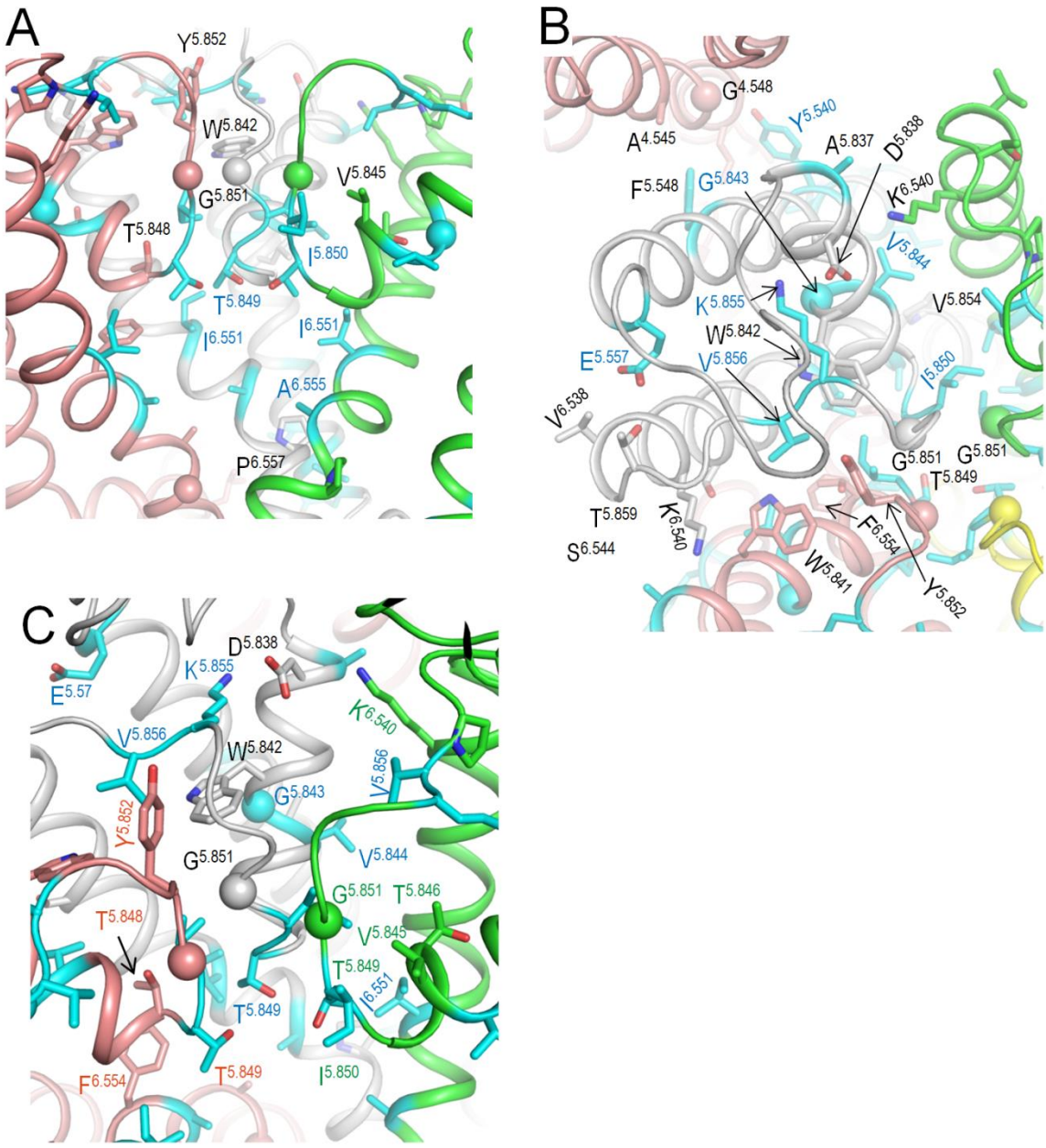

Figure 5. Close-up views of contacts in the extracellular part of Kv7.1 from Figure 4. WTRs involved in intersegment contacts (Table 4) are shown as sticks and CA atoms of glycines as spheres. WTRs of LP-reclassified VUSs (Table 3) are shown with cyan carbons. Their WTR contacts with ClinVar-listed variants are shown with carbons colored as respective ribbons. **A.** View from the pore at the selectivity filter region. **B.** Extracellular view at contacts involving P-loops. **C.** View from the pore on contacts involving P-loop.

The second category of contacts includes 16 WTRs of 26 LP-reclassified VUSs and 25 partner WTRs of 35 ClinVar reported VUSs (Table 5). Among the contact partners, 13 WTRs have 18 VUSs that we also reclassified as LP variants (Table 4). The fact that VUSs of both partners in such contacts were independently reclassified as LP variants by AlphaMissense and paralogue annotation methods further justifies LP reclassifications for respective VUSs making them promising objects for future functional analyses.

 doi:10.20944/preprints202506.0195.v1

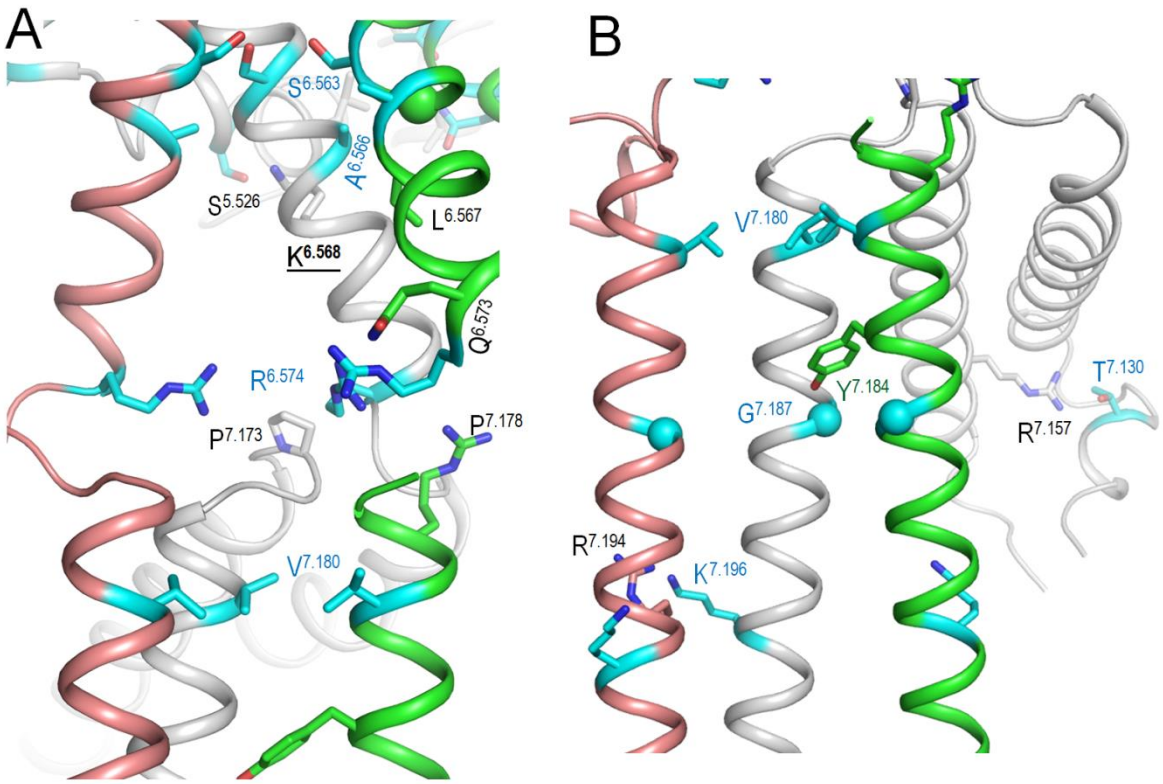

Figure 6. Close-up views of contacts in the cytoplasmic part of Kv7.1 from Figure 4. A. View at the border between transmembrane and cytoplasmic domains. **B**. View at the lower part of the cytoplasmic domain. WTRs with LP-reclassified VUSs are shown with cyan carbons.

The third category of contacts includes 15 WTRs of 20 LP-reclassified VUSs and 16 contact-partner WTRs for which 26 variants are reported in ClinVar as either CIP variants or their germline classification is not provided (Table 6). We suggest a damaging potential of the CIP variants because at least one submitter reported likely pathogenicity of the variant and respective WTR is contacting WTR with LP-reclassified VUS.

Table 6. Intersegment contacts [a] between WTRs of LP-reclassified VUSs and WTRs of CIP or NP variants [b].

VUS → LP	Contact [c]		VUS → LP	Contact	
V$^{164/A2.544}$A	S$^{209/A3.557}$P	NP	I$^{313/A5.850}$F	G$^{314/B5.851}$C/A	NP
A$^{223/A4.542}$T	Y$^{278/B5.551}$H	NP		T$^{309/B5.846}$S/R	NP
Q$^{260/A5.533}$H	L$^{236/D4.555}$R/P	CIP		V$^{308/B5.845}$D	NP
T$^{264/A5.537}$S	L$^{236/D4.555}$R/P	CIP	K$^{318/A5.855}$N	D$^{301/A5.838}$V	CIP
	L$^{233/D4.552}$P	CIP	I$^{337/A6.551}$M	T$^{311/D5.848}$A	NP
Y$^{267/A5.540}$F	L$^{233/4.552}$P	CIP		T$^{311/D5.848}$I	CIP
F$^{275/A5.548}$L	A$^{226/D4.545}$V	CIP	A$^{341/A6.555}$T	A$^{344/D6.558}$T/G	CIP
E$^{284/A5.557}$G	T$^{322/5.859}$K	CIP	S$^{349/A6.563}$A/L	S$^{349/B,D6.563}$P	CIP
	F$^{296/5.611}$S	CIP	A$^{352/A6.566}$P/D	S$^{349/B6.563}$P	CIP
T$^{312/A5.849}$S	I$^{337/A6.551}$F	CIP		G$^{350/B6.564}$V	CIP
			T$^{391/A7.030}$P	R$^{518/A7.157}$G	CIP

[a] In the cryoEM structure of hKv7.1 (PDB ID: 8sin) with voltage sensor in the down state (Mandala and MacKinnon, 2023); [b] ClinVar Data of 4-Mar-2025.

 doi:10.20944/preprints202506.0195.v1

Table 7. CryoEM structure [a] with activated VSDs: intersegment contacts of WTRs in VSD and S5 [b].

VUS → LP	Contact [c]	
C136/A1.553F	M159/2539L	VUS
S140/A1.557R	Q260/A5.533H	VUS → LP
V164/A2.544A	M210/3558T/I	VUS
E170/A2.550G	H240/4.559Q	VUS → LP
	V129/1546I/G/A	VUS
D202/A3.550V	H240/4.559Q	VUS → LP
L239/4.558V	Y267/A5.540F	VUS → LP
	F275/A5.548S/L	VUS → LP
H240/4.559Q/R	E170/A2.550G	VUS → LP
	D202/A3.550H	VUS → LP
V241/4.560I	Y267/5.540F	VUS
Y267/A5.540F	V241/4.560I	VUS → LP
	L239/4.558V	VUS → LP
F275/A5.548L	L239/4.558V	VUS → LP

[a] In the cryoEM structure of hKv7.1 (PDB ID: 8sik) with voltage sensor in the up state (Mandala and MacKinnon, 2023); [b] ClinVar Data of 4-Mar-2025; [c] CIP, Conflicting interpretations of pathogenicity; NP, data not provided.

2.8. Re-Classifying KCNE1 VUSs with High ClinPred Score and ClinVar-Reported Variants in Sequentially Matching Positions of Paralogues

KCNE1 association with Kv7.1 is important for normal heart rhythm, for reviews see (Wrobel et al., 2012; Sanguinetti and Seebohm, 2021). As of March 2025, over 600 variants of KCNE1 are reported in ClinVar, but only three missense variants (T7I, M1L and G52R) are classified as pathogenic. Among four known KCNE1 paralogs (KCNE2, KCNE3, KCNE4 and KCNE5), only KCNE2 contains 5 P/LP variants, while for other paralogues only VUSs are reported. Therefore, the paralogues annotation method for KCNE subunits is less reliable than for Kv channels. Nevertheless, ClinPred and the paralogues annotations consensually predicted likely pathogenicity of 34 VUSs for 21 WTRs in KCNE1 (Table 8). Among the 34 VUSs, 20 variants were explored in a recent high-throughput functional study of 68 KCNE1 variants (Vanoye et al., 2025), and for most of these the pick current decrease in the KCNQ1-KCNE1 assembly is reported (Table 8). These experimental data confirm reliability of our bioinformatics approach to predict likely pathogenicity of KNCE1 variant.

2.9. AF3 Model of Kv7.1 with KCNE1

In lack of cryoEM structures of Kv7.1-KCNE1, we created an AF3 model of complex Kv7.1-KCNE1 and MC-minimized its energy with rigid backbones (Figure 7). In this model, the large N-terminal portion of a single KCNE1 folded up to fill the space between two VSDs, while the smaller C-terminal part extended to the cytoplasm. WTRs of pathogenic variants M1L, T7I and G52R are shown as blue spheres. KCNE1 VUSs reclassifies as LP variants (Table 8) are shown as sticks in close-up views of Figure 7. Among multiple Kv7.1 WTRs that form contacts with KCNE1, six are known P/LP variants and several others are LP-reclassified VUSs (Table 3). Since these data alone are insufficient to prove our AF3 model of Kv7.1-KCNE1, we compared the model with the cryoEM structure of KCNE3-bound KV7.1 as described in next section.

 doi:10.20944/preprints202506.0195.v1

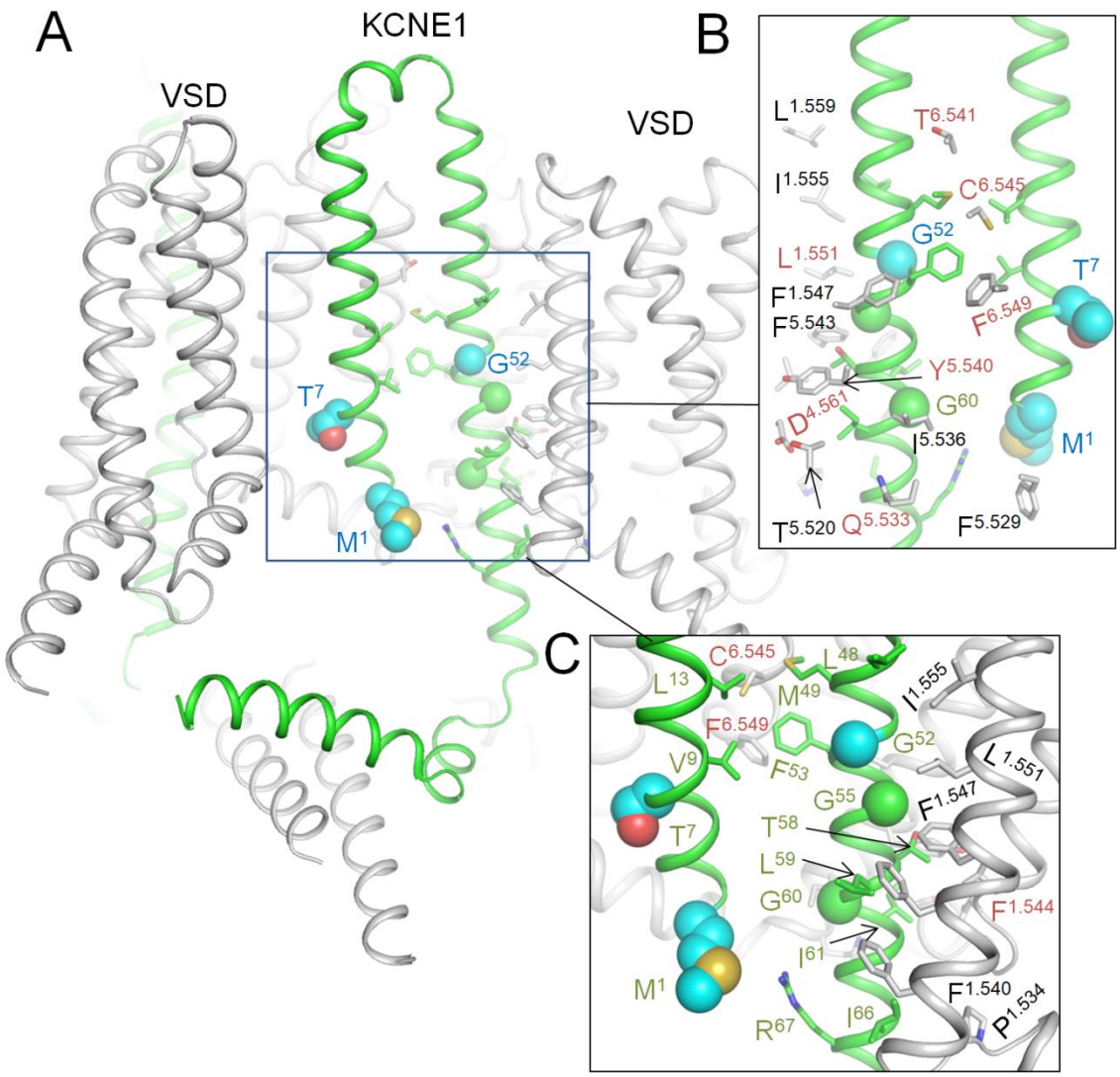

Figure 7. AF3 model of KCNE1-bound hNav7.1. **A.** Membrane view. WTRs of ClinVar reported KCNE1 pathogenic missense variants are shown as spheres with cyan carbons. **B, C.** Close-up views of KCNE1 contacts with Kv7.1. Backbones of Kv7.1 are not shown for clarity in panel *B*. KCNE1 WTRs with LP-reclassified variants (Table 8) are shown with green carbons. Kv7.1 residues that contact KCNE1 are shown with gray carbons. Residues listed in ClinVar are marked with red labels (Table 9).

2.10. CryoEM Structure of KCNE3-Bound Kv7.1

Kv7.1 co-assembles with KCNE3 in non-excitable cells (Abbott, 2016; Sun and MacKinnon, 2020), but there are evidence that such complexes are also expressed in human heart, especially in disease heart (Lundquist et al., 2005). KCNE1 and KCNE3 sequences are very different (Figure 8A), but there is sequence similarity in the middle part where KCNE3, which is resolved in the cryoEM structure (6v01) of KCNE3-bound Kv7.1 (Sun and MacKinnon, 2020) where the TM helix of KCNE3 is bound between S1 of VSD and extracellular parts of helices S5 and S6 (Figure 8B). In 3D-aligned cryoEM structure of Kv7.1-KCNE3 and AF3 model of Kv7.1-KCNE1, the TM part of KCNE3 helix (M^{60} to T^{80}) overlaps with KCNE1 helix from L^{45} to I^{66} (Figure 8C). It should be noted that the full-fledged cryoEM structure and the AF3 model are 3D-aligned by minimizing RMS deviations of sequentially matching CA atoms in helices P1 (see Methods) rather than sequentially matching CA atoms in the KCNE TM helices (Figure 8A). The perfect 3D match of the TM helices validates position of respective KCNE1 TM helix in our AF3 model (Figure 7).

 doi:10.20944/preprints202506.0195.v1

A

```
KCNE1      MILSNTTAVTPFLTKLWQETVQ--------------------QGGNMSGLARRSPRSSD     39
KCNE3      --MET-----TNGTETWYESLHAVLKALNATLHSNLLCRPGPGLGPDNQTEERRASLPGR     53
             :..        *: * *:::                          * : .   **:   .

KCNE1      GKLEALYVLMVLGFFGFFTLGIMLSYIRSKKLEHSNDPFNVYIESDAWQEKDKAYVQARV     99
KCNE3      DDNSYMYILFVMFLFAVTVGSLILGYTRSRKVDKRSDPYHVYIKNRVSMI----------     103
           .. . :*:*:*: :*.. . .::*.* **:*::: .**::***:. .

KCNE1      LESYRSCYVVENHLAIEQPNTHLPETKPSP     129
KCNE3      ------------------------------     103
```

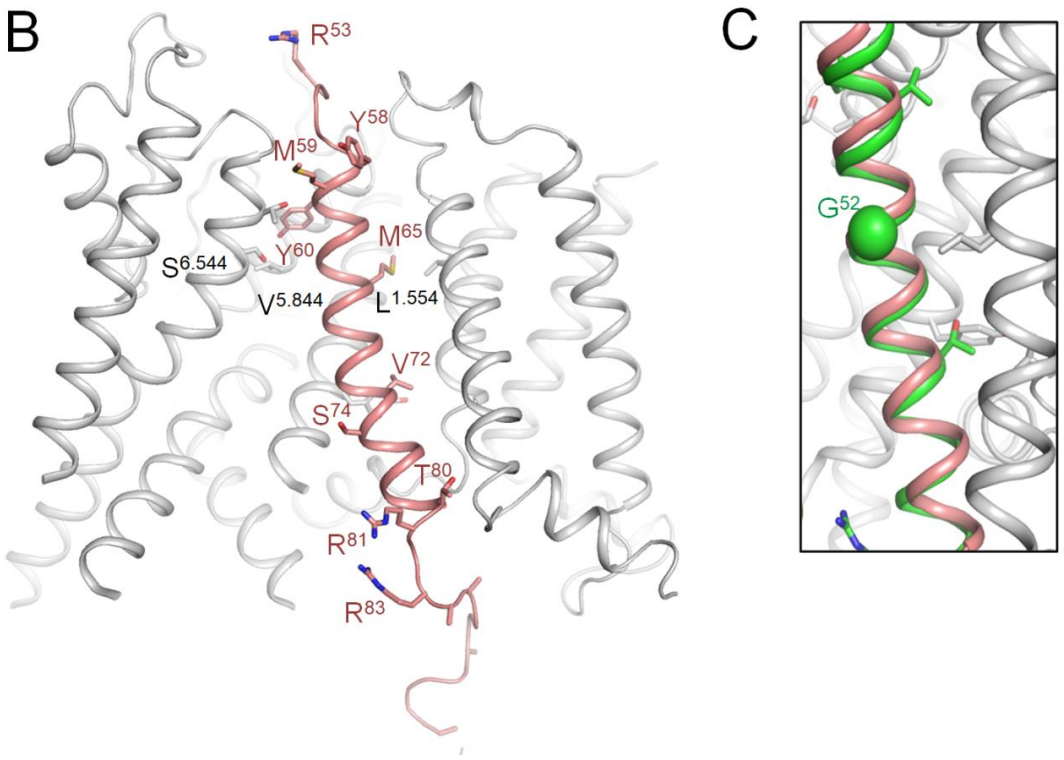

Figure 8. KCNE3 bound Kv7.1 (6v01) vs. AF3 model of KCNE1 bound Kv7.1. A. Sequence alignment of KCNE1 and KCNE3. TM helix of KCNE3 in the cryoEM structure (Y^{58}-T^{80}, orange) and TM helix in the AF3 model (A^{44}-I^{66}, green) have six identical and 12 similar residues. **B.** CryoEM structure of Kv7.1 (gray) with resolved part of KCNE3 (brown). Shown are KCNE3 WTRs with ClinVar reported P/LP variants (Table 8) and WTRs of their Kv7.1 contacts with LP-reclassified VUSs (Table 3). **C.** TM helix of KCNE1 in the AF3 model (green) matches KCNE3 helix (brown) in the cryoEM structure (6v01).

Table 8. KCNE1 VUSs reclassified as LP variants.

VUS	Cs	Functional Study [a]	ClinPred	Paralog
S28L	0.6	Smaller current	0.818	KCNE5-VUS:D44H
R32C	0.8	faster activation	0.622	KCNE3-VUS:R47G,KCNE3-VUS:R47Q,KCNE3-VUS:R47W
P35S	0.4	faster activation	0.957	KCNE2-VUS:V41A
L48I	0.9	~ current	0.963	KCNE2-Disease:M54T,KCNE2-VUS:M54V
L48F	0.9	faster activation	0.808	KCNE2-Disease:M54T,KCNE2-VUS:M54V
L48P	0.9		0.999	KCNE2-Disease:M54T,KCNE2-VUS:M54V
M49T	0.7		0.958	KCNE5-VUS:L65F
F53L	0.8	~ current	0.756	KCNE2-VUS:M59I,KCNE5-VUS:F69V
F53C	0.8	Small current	0.996	KCNE2-VUS:M59I,KCNE5-VUS:F69V
G55R	0.8		0.994	KCNE2-VUS:S61P
T58P	0.6	Slower activation	0.982	NA-Disease:T58PP,KCNE3-VUS:V72G
T58A	0.6		0.987	NA-Disease:T58PP,KCNE3-VUS:V72G

 doi:10.20944/preprints202506.0195.v1

L59P	0.7	LoF	0.978	KCNE2-VUS:V65L,KCNE2-VUS:V65M,KCNE5-VUS:G75R
G60D	0.8	Small current	0.994	KCNE2-VUS:A66V,KCNE3-VUS:S74R,KCNE5-VUS:G76D
G60V	0.8		0.995	KCNE2-VUS:A66V,KCNE3-VUS:S74R,KCNE5-VUS:G76D
I61F	1		0.983	KCNE2-VUS:I67M
I66L	0.7		0.905	KCNE3-VUS:T80I
R67G	0.9	Small current	0.996	KCNE3-VUS:R81C
R67S	0.9	Small current	0.987	KCNE3-VUS:R81C
R67L	0.9	Small current	0.99	KCNE3-VUS:R81C
R67H	0.9	Small current	0.873	KCNE3-VUS:R81C
K69E	0.9		0.953	KCNE3-VUS:R83C,KCNE3-VUS:R83P,KCNE5-VUS:R85H
K70Q	0.9		0.977	KCNE3-VUS:K84E,KCNE5-VUS:K86E
K70M	0.9	Small current	0.994	KCNE3-VUS:K84E,KCNE5-VUS:K86E
K70E	0.9		0.983	KCNE3-VUS:K84E,KCNE5-VUS:K86E
L71V	0.4		0.956	KCNE2-Disease:R77W,KCNE3-VUS:V85A
E72K	0.4		0.984	KCNE5-VUS:V88D,KCNE5-VUS:V88I
H73R	0.6		0.931	KCNE2-VUS:H79R,KCNE5-VUS:E89K
S74W	0.4	Small current	0.998	KCNE2-VUS:S80P,KCNE3-VUS:R88C,KCNE3-VUS:R88H
S74P	0.4	Smaller current	0.629	KCNE2-VUS:S80P,KCNE3-VUS:R88C,KCNE3-VUS:R88H
Y81C	0.7	Smaller current	0.998	KCNE2-VUS:Y87C
I82M	0.4	Smaller current	0.885	KCNE3-VUS:I96S
I82V	0.4	Smaller current	0.978	KCNE3-VUS:I96S
I82F	0.4		0.993	KCNE3-VUS:I96S

[a] (Vanoye et al., 2025).

Table 9. AF3 model: KCNE1 variants with WTRs, which contact WTRs of ClinVar-reported Kv7.1 variants.

KCNE1 Variant	Classification	Current Change [a]	Contact with			
			KCNE1		Kv7.1	
M[1]L/I/R/T/K/V	P/VUS		R[67]G/S/L/H	VUS	F[256/5.529]	
L[48]I/F/P	VUS→ LP	~			I[138/1.555] L[142/1.559]	
M[49]T/I	VUS→ LP		L[13]R/P/V/M	NP	C[331/6.545]Y T[327/6.541]D	VUS → LP VUS
G[52]R/ V/E/A	P/NP	R ↓			L[134/1.551]P	CIP
F[53]L/C	VUS→ LP	C ↓ L ~	L[13]R/P/V/M V[95]I	NP VUS	F[335/6.549]C F[270/5.543]	VUS → LP
G[55]R	VUS→ LP				L[134/1.551]P F[130/1.547]	CIP
T[58]P/A	VUS→ LP	P ↓			F[130/1.547] Y[267/5.540]F V[241/4.560]I	 VUS → LP VUS → LP
L[59]P	VUS→ LP				F[127/1.544]L F[123/1.540]	NP
G[60]D/V	VUS→ LP	D ↓			I[263/5.536]V	VUS
I[61]F	VUS→ LP				Y[267/5.540]F D[242/4.561]Y/N/E Q[260/5.533]H I[263/5.536]V T[247/5.520]	VUS → LP P/LP VUS → LP VUS
I[66]L	VUS→ LP				F[123/1.540] P[117/1.534]T/S/L	 LP
R[67]G/S/L/H	VUS→ LP	All ↓	M[1]L/I/R/T/K/V	P/NP		

[a] Measured for indicated variant (Vanoye et al., 2025).

 doi:10.20944/preprints202506.0195.v1

3. Methods

3.1. Sequence Data of Human Channels and Collection of Variants

The sequence of hKv7.1 was obtained from the UniProt database (UniProt, 2015) (accession number P51787). Paralogues of the hKv7.1 channel were identified using Ensembl (Dyer et al., 2025). Missense mutations for Kv7.1 and its paralogues were collected from three databases: Humsavar, Ensembl Variation (Boutet et al., 2016), and ClinVar (Landrum et al., 2016). Only P or LP variants were extracted from Ensembl Variation, ClinVar and Humsavar. VUSs were also obtained from ClinVar. Common benign (neutral) variants, along with their minor allele frequencies (AF), were sourced from the population database gnomAD (Karczewski et al., 2020). Variants with AF > 0.00001 that are not present in ClinVar were considered benign (Walsh et al., 2017; Kaltman et al., 2018). The total number of collected P/LP, VUS, and common neutral variants is given in Table 1. All variants were compiled into a comprehensive dataset (Table S1).

3.2. Topology of the Kv7.1 Channel

The hKv7.1 regions were defined in accordance with the UniProt entry P51787. The pore-forming α1 subunit of Kv7.1 assembles from four subunits. A large cytoplasmic domain plays critical roles in subunit assembly, interactions with regulatory proteins, and modulation of channel function (Haitin et al., 2009).

3.3. Multiple Sequence Alignment and Paralogue Annotation

The paralogue annotation method identifies P/LP missense variants by transferring annotations across families of related proteins (Walsh et al., 2014). Previously, we applied a modified version of this method to predict P/LP variants for channels hNav1.5 (Tarnovskaya et al., 2020), hCav1.2 (Tarnovskaya et al., 2021), and TRPM4 (Tarnovskaya et al., 2023). Here we used the same approach to predict P/LP variants for VUSs of hKv7.1.

For each paralogue channel, P/LP variants were collected. The amino acid sequences of hKv7.1 and its paralogue channels were aligned using the multiple sequence alignment program Tcoffee (Sievers et al., 2011). Proteins lacking P/LP variants were excluded from the alignment (Niroula and Vihinen, 2016). Since disease-causing mutations tend to occur at evolutionarily conserved positions, we computed position-specific conservation scores (Cs), which range from 0 (no conservation) to 1 (identical), with Cs=0.8 indicating high conservation. These scores reflect the conservation of physicochemical properties (small, polar, hydrophobic, tiny, charged, negative, positive, aromatic, aliphatic, and proline) in the alignment (Livingstone and Barton, 1993). Cs values were calculated using the Zvelebil method (Zvelebil et al., 1987), as implemented in the Amino Acid Conservation Calculation Service (Golicz et al., 2018). Variants occurring at positions with Cs > 0.3 were classified as P/LP variants.

3.4. Sequence-Based Prediction of Pathogenicity

Missense variants were annotated with scores from 29 algorithms (REVEL, VEST4, MVP, CADD, LIST.S2, VARITY_R, VARITY_ER, AlphaMissense, EVE, MPC, MVP, DANN, CenoCanyon, PrimateAI, DEOGEN2, M-CAP, MetaLR, MetaSVM, MetaRNN, FATHMM, PROVEAN, MutationAssessor, MutPred, PolyPhen2-HVAR, PolyPhen2-HDIV, SIFT, SIFT4G, LRT, MutationTaster), which were obtained from the dbNSFPv4.5 database (Liu et al., 2020). To generate binary predictions (Damaging/Tolerated), we used thresholds determined as the optimal pathogenicity threshold from the AUC-ROC curve (Table 2).

The ‘probably damaging’ and ‘possibly damaging’ classes predicted by Polyphen were merged into a single ‘damaging’ class. For results from the MutationAssessor server, which subdivides mutants into four categories, we treated categories high (‘H’) or medium (‘M’) as ‘Damaging’, and categories low (‘L’) or neutral (‘N’) as ‘Tolerated’.

 doi:10.20944/preprints202506.0195.v1

The overall prediction performance of the 29 methods was assessed by calculating sensitivity, specificity, Matthews Correlation Coefficient (MCC), and accuracy (ACC) as follows:

$$\text{Sensitivity} = \frac{TP}{TP + FN}; \quad (1)$$

$$\text{Specificity} = \frac{TN}{TN + FP}; \quad (2)$$

$$\text{MCC} = \frac{TP \times TN - FP \times FN}{\sqrt{(TP + FP)(TP + FN)(TN + FP)(TN + FN)}}; \quad (3)$$

$$\text{ACC} = \frac{TP + TN}{TP + FP + TN + FN}. \quad (4)$$

The following abbreviations are used in these equations:

TP (true positive) is the number of disease-causing variants correctly predicted to be pathogenic;

FN (false negative) is the number of disease-causing variants incorrectly predicted as tolerated;

TN (true negative) is the number of neutral variants correctly predicted as tolerated;

FP (false positive) is the number of neutral variants incorrectly predicted as pathogenic;

MCC is a correlation coefficient between the observed and predicted binary classification, ranging from -1 (total disagreement between prediction and observation) to 1 (perfect prediction)

For the test dataset, we selected common neutral and P/LP variants from our comprehensive dataset (Supplementary Table S1). We also calculated the area under the ROC (Receiver Operating Characteristic) curve (AUC) using the pROC library in the R programming language. ROC curves were generated by plotting sensitivity against (1 – specificity) at each threshold for each algorithm. The AUC can range from 0 (completely random) to 1 (perfectly correct prediction). The absence of a variant annotation negatively impacts prediction accuracy. Therefore, we included only those algorithms that predicted the pathogenicity of over 30% of variants in our dataset (Table S1).

3.5. Molecular Modeling

All computations were performed with the freely available ZMM program (www.zmmsift.ca). Energy was calculated using the AMBER force field (Weiner et al., 1986) with environment- and distance-dependent dielectric function (Garden and Zhorov, 2010). Energy was optimized with Monte Carlo (MC) energy minimizations (Li and Scheraga, 1987) in the space of generalized coordinates (Zhorov, 1981). We used AlphaFold3 (AF3) server (https://alphafold.ebi.ac.uk) to predict complexes of hKv7.1 with the full-fledged KCNE1 subunit. CryoEM structures of Kv7.1 with the activated and deactivated VSDs as well as AF3 models were imported by the ZMM program and side chain conformations were MC-minimized with rigid backbones. MCM trajectories were terminated when the last 100th energy minimization did not improve the protein energy. All structures were 3D-aligned by minimizing the root mean square deviations of C^{α} atoms in P1 helices against a reference crystal structures of the chimeric potassium channels Kv1.2-Kv2.1 channel (PDB ID: 2R9R), the first eukaryotic P-loop potassium channels whose crystal structure was obtained with the resolution below 2.5 Å (Long et al., 2007).

Intersegment contracts are defined as those where two sidechains are within 5Å from each other. Such contacts were automatically identified by ZMM in MC-minimized structures. We used PyMol (Schrödinger, New York, NY, USA) to visualize cryoEM structures and AF3 models of the Kv7.1 channel and its complex with KCNE1. Other details of computations may be found elsewhere (Zhorov, 2021).

4. Conclusions

In this study, we compiled a comprehensive dataset encompassing known pathogenic and likely pathogenic variants in the hKv7.1 channel and its 14 paralogues. Our analysis identified

 doi:10.20944/preprints202506.0195.v1

AlphaMissense as the top-performing bioinformatics tool for predicting likely pathogenic/pathogenic (LP/P) variants in Kv channels. Using AlphaMissense and the paralogue annotation method, we consensually predicted 79 VUSs of Kv7.1 as LP variants. We also used bioinformatics to predict LP status for 34 KCNE1 VUSs. Many wild type residues (WTRs) of LP-reclassified variants make state-dependent intersegments contacts with WTRs of known P/LP variants or reclassified LP variants in cryo-EM structures or AlphaFold-3 models, suggesting atomic mechanisms of the variants' dysfunction. Respective variants of Kv7.1 and KCNR1 are promising objects for future functional analyses.

Supplementary Materials: The following supporting information can be downloaded at the website of this paper posted on Preprints.org.

Author Contributions: Methodology, Svetlana I Tarnovskaya and Boris S Zhorov; Software, Boris S Zhorov; Validation, Boris S Zhorov; Investigation, Svetlana I Tarnovskaya and Boris S Zhorov; Data curation, Svetlana I Tarnovskaya; Writing – original draft, Svetlana I Tarnovskaya; Writing – review & editing, Boris S Zhorov; Visualization, Boris S Zhorov; Supervision, Boris S Zhorov; Project administration, Boris S Zhorov; Funding acquisition, Boris S Zhorov.

Funding: This research was funded by Natural Sciences and Engineering Research Council of Canada (RGPIN-2020-07100) and Ongoing funding of the Sechenov Institute, RAS (N.A.).

Data Availability Statement: The original contributions presented in this study are included in the article/supplementary material. Further inquiries can be directed to the corresponding author.

Acknowledgments: The study was supported by the Natural Sciences and Engineering Research Council of Canada (RGPIN-2020-07100) to BSZ and ongoing funding of the Sechenov Institute. We thank Dr. Vyacheslav Korkosh for administrating database www.plic-3da.

Conflicts of Interest: The authors declare no conflict of interest.

Abbreviations

AUC	Area Under the ROC Curve
CIP	Conflicting interpretation of pathogenicity
LQTS	Long QT syndrome
MC	Monte Carlo
NP	germline classification of pathogenicity is not provided
P/LP	Pathogenic/Likely pathogenic variant
PLIC	P-loop ion channels
TM	Transmembrane
ROC	Receiver Operating Characteristic
VSD	Voltage-sensing domain
VUS	Variant of Unknown clinical significance
WTR	Wild-Type Residue

References

Abbott GW (2016) KCNE1 and KCNE3: The yin and yang of voltage-gated K(+) channel regulation. *Gene* **576**(1 Pt 1): 1-13.

Abbott JW (2014) Biology of the KCNQ1 Potassium Channel. *New Journal of Science* **2014**(237431): 1-26.

Albert CM, et al. (2010) Common variants in cardiac ion channel genes are associated with sudden cardiac death. *Circulation Arrhythmia and electrophysiology* **3**(3): 222-229.

Bains S, et al. (2024) KCNQ1 suppression-replacement gene therapy in transgenic rabbits with type 1 long QT syndrome. *European heart journal* **45**(36): 3751-3763.

Barro-Soria R, Perez ME and Larsson HP (2015) KCNE3 acts by promoting voltage sensor activation in KCNQ1. *Proc Natl Acad Sci U S A* **112**(52): E7286-7292.

 doi:10.20944/preprints202506.0195.v1

Bellocq C, et al. (2004) Mutation in the KCNQ1 gene leading to the short QT-interval syndrome. *Circulation* **109**(20): 2394-2397.

Boutet E, et al. (2016) UniProtKB/Swiss-Prot, the Manually Annotated Section of the UniProt KnowledgeBase: How to Use the Entry View. *Methods in molecular biology (Clifton, NJ)* **1374**: 23-54.

Brewer KR, et al. (2025) Integrative analysis of KCNQ1 variants reveals molecular mechanisms of type 1 long QT syndrome pathogenesis. *Proc Natl Acad Sci U S A* **122**(8): e2412971122.

Campuzano O, et al. (2015) Genetics of channelopathies associated with sudden cardiac death. *Global cardiology science & practice* **2015**(3): 39.

Chen YH, et al. (2003) KCNQ1 gain-of-function mutation in familial atrial fibrillation. *Science* **299**(5604): 251-254.

Dyer SC, et al. (2025) Ensembl 2025. *Nucleic Acids Res* **53**(D1): D948-D957.

Garden DP and Zhorov BS (2010) Docking flexible ligands in proteins with a solvent exposure- and distance-dependent dielectric function. *Journal of computer-aided molecular design* **24**(2): 91-105.

Gigolaev AM, et al. (2025) Golden Gate cloning enables efficient concatemer construction for biophysical analysis of heterozygous potassium channel variants from patients with epilepsy. *International Journal of Biological Macromolecules* **In Press**.

Golicz A, et al. (2018) AACon: A Fast Amino Acid Conservation Calculation Service. *Submitted paper*.

Haitin Y, et al. (2009) Intracellular domains interactions and gated motions of I(KS) potassium channel subunits. *The EMBO journal* **28**(14): 1994-2005.

Hateley S, et al. (2021) The history and geographic distribution of a KCNQ1 atrial fibrillation risk allele. *Nature communications* **12**(1): 6442.

Huang H, et al. (2018) Mechanisms of KCNQ1 channel dysfunction in long QT syndrome involving voltage sensor domain mutations. *Science advances* **4**(3): eaar2631.

Jespersen T, Grunnet M and Olesen SP (2005) The KCNQ1 potassium channel: from gene to physiological function. *Physiology* **20**: 408-416.

Kaltman JR, Evans F and Fu Y-P (2018) Re-evaluating pathogenicity of variants associated with the long QT syndrome. *Journal of Cardiovascular Electrophysiology* **29**(1): 98-104.

Karczewski KJ, et al. (2020) The mutational constraint spectrum quantified from variation in 141,456 humans. *Nature* **581**(7809): 434-443.

Kasuya G and Nakajo K (2022) Optimized tight binding between the S1 segment and KCNE3 is required for the constitutively open nature of the KCNQ1-KCNE3 channel complex. *eLife* **11**.

Kekenes-Huskey PM, et al. (2022) Mutation-Specific Differences in Kv7.1 (KCNQ1) and Kv11.1 (KCNH2) Channel Dysfunction and Long QT Syndrome Phenotypes. *International journal of molecular sciences* **23**(13).

Kiper AK, et al. (2024) KCNQ1 is an essential mediator of the sex-dependent perception of moderate cold temperatures. *Proc Natl Acad Sci U S A* **121**(25): e2322475121.

Korkosh VS, et al. (2021) Intersegment Contacts of Potentially Damaging Variants of Cardiac Sodium Channel. *Frontiers in pharmacology* **12**: 756415.

Landrum MJ, et al. (2016) ClinVar: Public archive of interpretations of clinically relevant variants. *Nucleic Acids Research* **44**(D1): D862-D868.

Li Z and Scheraga HA (1987) Monte Carlo-minimization approach to the multiple-minima problem in protein folding. *Proceedings of the National Academy of Sciences of the United States of America* **84**(19): 6611-6615.

Liu X, et al. (2020) dbNSFP v4: a comprehensive database of transcript-specific functional predictions and annotations for human nonsynonymous and splice-site SNVs. *Genome Med* **12**(1): 103.

Livingstone CD and Barton GJ (1993) Protein sequence alignments: a strategy for the hierarchical analysis of residue conservation. *Computer applications in the biosciences : CABIOS* **9**(6): 745-756.

Long SB, et al. (2007) Atomic structure of a voltage-dependent K+ channel in a lipid membrane-like environment. *Nature* **450**(7168): 376-382.

Lundquist AL, et al. (2005) Expression of multiple KCNE genes in human heart may enable variable modulation of I(Ks). *Journal of molecular and cellular cardiology* **38**(2): 277-287.

Mandala VS and MacKinnon R (2023) The membrane electric field regulates the PIP(2)-binding site to gate the KCNQ1 channel. *Proc Natl Acad Sci U S A* **120**(21): e2301985120.

 doi:10.20944/preprints202506.0195.v1

Niroula A and Vihinen M (2016) Variation Interpretation Predictors: Principles, Types, Performance, and Choice. *Human Mutation* **37**(6): 579-597.

Phul S, et al. (2022) Predicting the functional impact of KCNQ1 variants with artificial neural networks. *PLoS computational biology* **18**(4): e1010038.

Rothenberg I, et al. (2016) Structural interplay of K(V)7.1 and KCNE1 is essential for normal repolarization and is compromised in short QT syndrome 2 (K(V)7.1-A287T). *HeartRhythm case reports* **2**(6): 521-529.

Sachyani D, et al. (2014) Structural basis of a Kv7.1 potassium channel gating module: studies of the intracellular c-terminal domain in complex with calmodulin. *Structure* **22**(11): 1582-1594.

Sanguinetti MC and Seebohm G (2021) Physiological Functions, Biophysical Properties, and Regulation of KCNQ1 (K(V)7.1) Potassium Channels. *Advances in experimental medicine and biology* **1349**: 335-353.

Sievers F, et al. (2011) Fast, scalable generation of high-quality protein multiple sequence alignments using Clustal Omega. *Mol Syst Biol* **7**: 539.

Sun J and MacKinnon R (2017) Cryo-EM Structure of a KCNQ1/CaM Complex Reveals Insights into Congenital Long QT Syndrome. *Cell* **169**(6): 1042-1050 e1049.

Sun J and MacKinnon R (2020) Structural Basis of Human KCNQ1 Modulation and Gating. *Cell* **180**(2): 340-347 e349.

Tarnovskaya SI, et al. (2020) Predicting novel disease mutations in the cardiac sodium channel. *Biochem Biophys Res Commun* **521**(3): 603-611.

Tarnovskaya SI, Kostareva AA and Zhorov BS (2021) L-Type Calcium Channel: Predicting Pathogenic/Likely Pathogenic Status for Variants of Uncertain Clinical Significance. *Membranes (Basel)* **11**(8).

Tarnovskaya SI, Kostareva AA and Zhorov BS (2023) In silico analysis of TRPM4 variants of unknown clinical significance. *PLoS One* **18**(12): e0295974.

Tikhonov DB, Korkosh VS and Zhorov BS (2025) 3D-aligned tetrameric ion channels with universal residue labels for comparative structural analysis. *Biophysical journal* **124**(2): 458-470.

UniProt C (2015) UniProt: a hub for protein information. *Nucleic Acids Res* **43**(Database issue): D204-212.

Vanoye CG, et al. (2018) High-Throughput Functional Evaluation of KCNQ1 Decrypts Variants of Unknown Significance. *Circulation Genomic and precision medicine* **11**(11): e002345.

Vanoye CG, et al. (2025) Functional profiling of KCNE1 variants informs population carrier frequency of Jervell and Lange-Nielsen syndrome type 2. *bioRxiv*.

Walsh R, et al. (2014) Paralogue annotation identifies novel pathogenic variants in patients with Brugada syndrome and catecholaminergic polymorphic ventricular tachycardia. *Journal of medical genetics* **51**(1): 35-44.

Walsh R, et al. (2017) Reassessment of Mendelian gene pathogenicity using 7,855 cardiomyopathy cases and 60,706 reference samples. *Genet Med* **19**(2): 192-203.

Weiner SJ, et al. (1986) An all atom force field for simulations of proteins and nucleic acids. *Journal of computational chemistry* **7**(2): 230-252.

Wrobel E, Tapken D and Seebohm G (2012) The KCNE Tango - How KCNE1 Interacts with Kv7.1. *Frontiers in pharmacology* **3**: 142.

Wu X and Larsson HP (2020) Insights into Cardiac IKs (KCNQ1/KCNE1) Channels Regulation. *International journal of molecular sciences* **21**(24).

Zhorov BS (1981) Vector method for calculating derivatives of energy of atom-atom interactions of complex molecules according to generalized coordiantes. *J Struct Chem* **22**: 4-8.

Zhorov BS (2021) Possible Mechanism of Ion Selectivity in Eukaryotic Voltage-Gated Sodium Channels. *The journal of physical chemistry B* **125**(8): 2074-2088.

Zvelebil MJ, et al. (1987) Prediction of protein secondary structure and active sites using the alignment of homologous sequences. *J Mol Biol* **195**(4): 957-961.

 doi:10.20944/preprints202506.0195.v1

disclaim responsibility for any injury to people or property resulting from any ideas, methods, instructions or products referred to in the content.